



# Time-efficient simulations of fighter aircraft weapon bay

Karthick Rajkumar<sup>1</sup> · Eike Tangermann<sup>1</sup> · Markus Klein<sup>1</sup> · Sebastian Ketterl<sup>2</sup> · Andreas Winkler<sup>2</sup>

Received: 1 April 2022 / Revised: 22 August 2022 / Accepted: 25 August 2022 / Published online: 6 January 2023  
© The Author(s) 2023

## Abstract

A cavity flow exhibits aero-acoustic coupling between the separated shear layer and reflecting waves within the walls of the cavity, which leads to emergence of dominant modes. It is of primary importance that this flow mechanism inside the cavity is understood to provide insights and control the relevant parameters and that it can be properly predicted using state-of-the-art CFD tools. In this study, an open-cavity configuration with doors attached on the sides and a length-to-depth ratio of 5.7 have been studied numerically using the TAU code developed by the German Aerospace Center for transonic flows with three simulation methods such as DES with wall functions and SST-SAS with resolved wall flow or wall function techniques. The free-stream conditions investigated are Mach number (Ma) 0.8 with Reynolds number (Re)  $12 \times 10^6$ . The Rossiter modes occurring in the cavity due to the acoustic feedback mechanism have been numerically computed and validated. The SST-SAS model is around 90% more computationally efficient compared to the hybrid RANS-LES model providing excellent accuracy in predicting the Rossiter modes. The SST-SAS model with wall functions is 50% more computationally efficient than wall-resolving SAS simulations showing good behaviour in predicting modal frequencies and shapes, with further scope for improvement in the spectral magnitude levels.

**Keywords** Cavity flow · Rossiter modes · Hybrid RANS-LES · Scale-adaptive simulation (SAS)

## Abbreviations

CFL	Courant–Friedrichs–Lewy number
DES	Detached-Eddy simulation
DES-WF	Detached-Eddy simulation with wall function approach
DNS	Direct numerical simulation
FFT	Fast-Fourier transform
FVS	Flux vector split
IDDES	Improved delayed detached-Eddy simulation

LES	Large Eddy simulation
NS	Navier–Stokes
RANS	Reynolds averaged Navier–Stokes
RMS	Root mean square
SA	Spalart–Allmaras one-equation model
SA-neg	Spalart–Allmaras one-equation model with negative turbulent viscosity correction
SPL	Sound pressure level
SST	Shear stress transport
SAS	$k-\omega$ SST model with SAS correction term using wall integration approach
SAS-WF	$k-\omega$ SST model with SAS correction term using wall function approach
URANS	Unsteady Reynolds averaged Navier–Stokes

✉ Karthick Rajkumar  
karthick.rajkumar@unibw.de

Eike Tangermann  
eike.tangermann@unibw.de

Markus Klein  
markus.klein@unibw.de

Sebastian Ketterl  
sebastian.ketterl@airbus.com

Andreas Winkler  
andreas.dr.winkler@airbus.com

<sup>1</sup> Department of Aerospace Engineering, University of the Bundeswehr Munich, 85577 Neubiberg, Bayern, Germany

<sup>2</sup> Division of Flight Physics, Airbus Defence and Space, 80577 Manching, Bayern, Germany

## List of symbols

$\alpha$	phase delay constant
AoA	Angle of attack (°)
$\beta$	Side slip angle (°)
$d$	Distance to the nearest wall (m)
$\Delta$	Maximum grid spacing (m)
$\Delta_x, \Delta_y, \Delta_z$	Grid spacing in $x, y, z$ directions (m)
$f$	Frequency (Hz)
$\gamma$	Adiabatic exponent

$\kappa$	Ratio of convection velocity of vortical structure to the free-stream velocity
$L$	Length of the cavity (m)
$L_x$	Distance of the local point from the leading edge of the cavity rig (m)
$L/D$	Length to depth ratio of the cavity
$L/W$	Length to width ratio of the cavity
$L_{vK}$	Von Karman length scale (m)
$m$	Rossiter mode number
$Ma$	Free stream Mach number
$\omega$	Vorticity (1/s)
$Q$	Q-criterion
$Re$	Reynolds number
$Re_x$	local Reynolds number
$\rho$	Density (kg/m <sup>3</sup> )
$\epsilon_v$	Turbulent destruction term
$P_v$	Turbulent production term
$U_\infty$	Free stream velocity (m/s)
$u, v, w$	Instantaneous velocity components in $x, y, z$ directions (m/s)
$W$	Width of the cavity (m)
$y^+$	Non-dimensional wall distance

## 1 Introduction

Historically, research of cavity flows has been done by aerospace companies, specifically for weapon bays. A cavity flow presents a complex unsteady flow and acoustic processes due to the shedding of separated shear layer from the front edge of the cavity. This causes severe limitations for operating weapon bays and landing gears, etc. In weapon bays, the deployment of stores could be improved by controlling the flow mechanisms existing inside the cavity which requires a fundamental understanding of cavity flow physics. Additionally at present, due to the requirement of stealth characteristics of the aircraft, the investigation of cavity flows has become even more crucial.

In general, there are closed, transitional and open-cavity flow type [1]. Categorization of cavity flow type can be based on several factors such as length-to-depth ratio ( $L/D$ ) and Mach number ( $Ma$ ). In the closed cavity configuration, the shear layer flow separates from the front edge of the cavity, loses its energy, and reattaches to the cavity before separating again. There exists two large-scale recirculations on either corners of the cavity. In the open flow cavity, there is one large-scale recirculation caused by the shear layer that carries enough energy to cross the length of the cavity. The shear layer in the open-cavity flow type impinges on the rear wall, which then acts as an acoustic source to initiate sustained flow oscillations inside the cavity. In the transitional cavity, the flow reattachment to the ceiling of the cavity is unstable.

There are many articles in the literature that show the effort to investigate the modal tones produced in the cavity. One explanation that is accepted by many authors is the Rossiter flow oscillation model (Eq. 1). Rossiter [2] postulated a semi-empirical model to estimate the dominant modal frequencies produced in the cavity. The model is based on the observations that the downstream convection of vortices from the shear layer generates aerodynamic disturbances, which then are excited by the reflected pressure waves from the rear wall produced by the shedding layer. This feedback process continues and leads to a self-sustained oscillation process

$$f = \frac{U_\infty}{L} \frac{m - \alpha}{Ma + 1/\kappa}. \quad (1)$$

Much of the cavity flow research has been experimental. The study by Rossiter [2] was one of the foremost studies that provided a solid understanding of the physics-based acoustic-flow dynamic interaction. The model by Rossiter (Eq. 1) is still widely used to predict the modes, particularly in the subsonic and transonic flow conditions. However, the model has shown some inaccuracies in supersonic flow conditions. Heller et al. [3] improved the Rossiter model by assuming that the speed of sound inside the cavity is equal to that in the stagnating freestream to extend its validity to supersonic flows as well. Handa et al. [4] have studied the generation and propagation of pressure waves experimentally and showed the periodic nature of them. The study explains the process by which the pressure waves are generated. It attempts to clarify the relationship between the shear-layer motion, pressure-wave generation, and the pressure oscillation inside the cavity.

After extensive wind-tunnel studies on the cavity, several attempts have been made to study the cavity flows numerically, mostly on the M219 cavity [5] to describe the flow physics inside the cavity and accordingly determine the resonant modes. Henderson et al. [6] carried out time-accurate simulations using the RANS  $k-\omega$  model and it has been shown that the models are unable to predict the broadband spectra. To determine both the narrowband and broadband spectra accurately, advanced turbulence resolving methods such as DES methods based on Spalart–Allmaras (SA) and  $k-\omega$  SST have been used [7].

Many of the numerical studies pertaining to cavity flows were based on the URANS approach. Chang et al. [8] studied 3D incompressible flow past an open cavity using the SA model. Although the predictions of the mean velocity field from the URANS and the scale-resolving simulation were similar, the study found that the URANS predictions show poor agreement with LES and experimental results for the turbulent quantities.

Woo et al. [9] studied the three-dimensional effects of supersonic cavity flow due to the variation of cavity aspect and width ratios using the RANS  $k-\omega$  turbulence model. The compressible NS equations were solved with the fourth-order Runge–Kutta method and FVS method with van Leer's flux limiter. The study concluded the oscillation mode 2 appeared as a dominant oscillation frequency regardless of the aspect ratio of the cavity in the two-dimensional flow and oscillation mode 1 and 2 appeared in three-dimensional cavities of small aspect ratios. With the increase in the aspect or the width ratios, only the modes 2 or 3 appeared as a dominant frequency.

It is understood that due to the nature of the URANS formulation, the method has an inherent inability to detect modes accurately. Therefore, a number of studies have been dedicated to scale-resolving turbulence models such as LES. The study by Larcheveque et al. [10] shows the accuracy of employing LES or DES methods for a 3D cavity case where doors are present and aligned vertically.

DES simulations are still expensive, whereas the scale-adaptive simulation (SAS) approach developed by Menter [11] has shown to provide results nearly as good as DES or LES. Girimaji et al. [12] evaluated the scale-adaptive simulation of M219 cavity flows for transonic flow conditions. The SAS results showed good agreement with the experimental data for the M219 cavity at a tenth of the time required for Detached-Eddy simulations. As the SAS simulations are yet quite expensive for use in the industrial design process, further reduction in the computational time is sought. Therefore, in the pursuit of reducing the computational effort for cavity simulations, the SAS simulations have been investigated using the wall function technique in this study and its merits and demerits have been outlined in terms of acoustic prediction.

In this study, a novel open-cavity configuration with opened doors at the sides [13] has been investigated numerically at transonic flow conditions using two scale-resolving methods namely, a hybrid RANS-LES method with wall function (DES-WF) and scale adaptive simulation (SAS). The scale-adaptive simulation was also carried out using

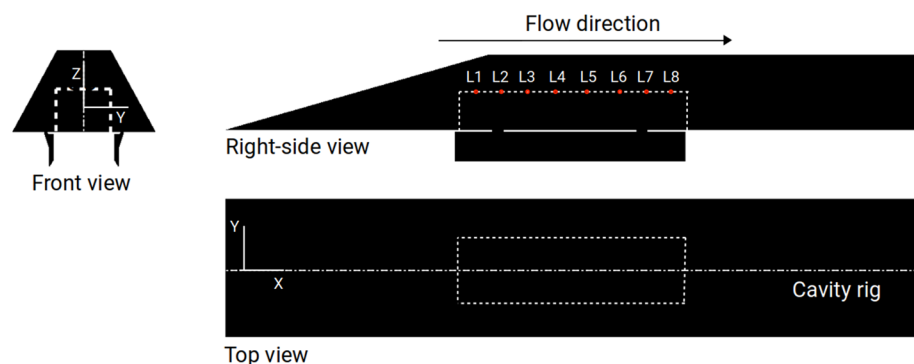
wall function technique (SAS-WF) to investigate the feasibility of simulating the cavity flows. The numerical simulations have been performed using the DLR-TAU computational fluid dynamics (CFD) code [14] under the flow conditions of  $Ma$  0.8 and  $Re$   $12 \times 10^6$ . The numerically computed RMS values and wall spectra have been validated against the experimental data, which have been made available for this study by Airbus Defence and Space [13].

## 2 Model configuration and mesh generation

The cavity configuration used in this study has dimensions of length-to-depth ratio ( $L/D$ ) 5.7 and length-to-width ratio ( $L/W$ ) 4.16 (see Fig. 1). The cavity is cut onto a flat side along the centre line of the cavity rig at a certain distance from the rig's sharp leading edge. Under the transonic flow condition of  $Ma = 0.8$  with the Reynolds number of the flow  $12 \times 10^6$ , the cavity is expected to exhibit resonance. The doors are placed on either side of the cavity with positive  $Z$  pointing into the cavity. The probe locations placed at equidistant locations along the cavity ceiling and are named L1 to L8, as shown in Fig. 1.

The cavity geometry has been spatially discretized with a mesh consisting of unstructured elements with tetrahedral, prism, hexahedral, and pyramid cells. A RANS model was used to estimate the integral length scale, and according to the estimates, cell sizes have been chosen appropriately during the meshing stage. Figure 2 shows the DES-WF mesh that is used for this study. In Fig. 2a, the overview of the mesh distribution is shown. As the motivation of the study is to investigate the flow mechanisms as efficient as possible in terms of computational time, only the region of interest has been meshed with the highest level of refinement, as shown in Fig. 2. By adapting the mesh proportion inside the cavity, as shown in Fig. 2b, one can save a significant number of mesh nodes. In the cavity geometry, a 50% reduction in the number of prism cells has the potential to reduce the total number of mesh nodes by almost 40%, which suggests that one can save a significant amount of computational time by

**Fig. 1** Model of the open cavity with side doors



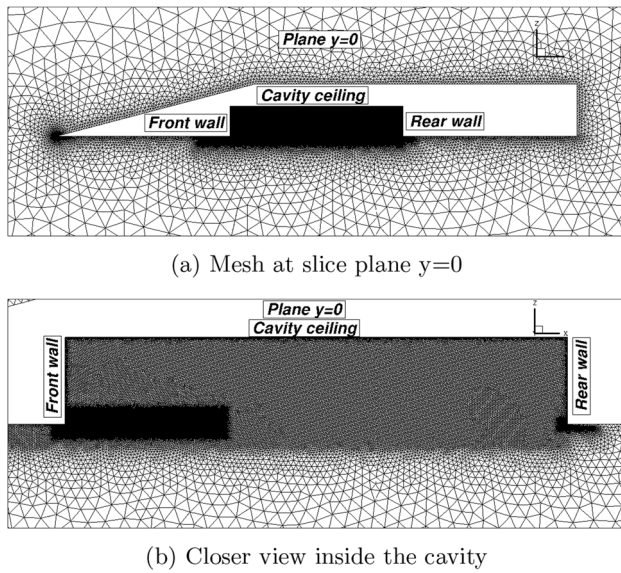


Fig. 2 Mesh distribution

reducing the number of prism layers while adopting a wall function technique. The model has been meshed in half and mirrored about the symmetry axis to avoid the asymmetric grid effects. The DES-WF mesh is composed of  $12.5 \times 10^6$  grid nodes. In the SAS mesh, the cell size in the shear layer and inside the cavity is almost double the cell size of the DES-WF mesh and contains around  $5 \times 10^6$  grid nodes. The number of mesh nodes in SAS-WF is about half of that of the SAS mesh. Moreover, a non-dimensional wall coordinate ( $y^+$ ) of more than 100 has been set along the walls of the cavity for DES-WF and SAS-WF cases.

### 3 Flow solver and turbulence modelling

The numerical simulations have been carried out in this study using the DLR-TAU code, a finite volume (FV) flow solver based on the compressible Navier–Stokes formulation developed by the German Aerospace Center (DLR) [14]. The popular RANS approach in industry for turbulence modelling loses a lot of intricate details in the flow field when it is employed to the unsteady cavity flow simulation. An alternative is an LES-based model, which resolves major part of the energy carrying eddies and model the isotropic sub-grid scales [15]. As the cavity configuration has a boundary layer developed on the cavity rig upstream of the cavity, which then leads to the shear layer formation, an LES model requires an uncompromised resolution of the boundary layer and a substantial computing time for this application. Therefore, the following numerical approaches for turbulence modelling are employed in this study.

### 3.1 Hybrid RANS-LES approach

In the author's previous work [16], the hybrid RANS-LES approach with wall resolved technique has been investigated and the first promising results of this cavity configuration have been published. In the present study, some of the numerical settings used in the previous study [16] have been optimised and the DES part of this study differentiates from the author's earlier work using matrix dissipation and adopting the wall function approach for the cavity flow in the current study. By applying matrix dissipation in this study, the artificial dissipation is reduced to prevent excessive damping of the resolved turbulent structures.

The SANeg-IDDES model [17] is based on the standard one-equation Spalart–Allmaras model, which models the transport equation for the eddy viscosity [18]

$$\frac{\partial}{\partial t}(\rho\tilde{\nu}) + \mathbf{u} \cdot \nabla(\rho\tilde{\nu}) = \nabla \cdot \left( \frac{\mu + \rho\tilde{\nu}}{\sigma} \nabla\tilde{\nu} \right) + \rho \frac{c_{b2}}{\sigma} (\nabla\tilde{\nu})^2 + P_{\nu} - \epsilon_{\nu}, \quad (2)$$

where the production term  $P_{\nu}$  and the destruction term  $\epsilon_{\nu}$  are

$$P_{\nu} = c_{b1}\rho\tilde{S}\tilde{\nu} \quad \text{and} \quad \epsilon_{\nu} = c_{w1}f_w\rho\left(\frac{\tilde{\nu}}{\tilde{d}}\right)^2. \quad (3)$$

This model represents the standard SA model, except that the length scale  $\tilde{d}$  in the destruction term is modified. In the SA model,  $d$  is the distance to the nearest wall. In the IDDES model [19] that is used in this study,  $d$  is replaced with  $\tilde{d}$ , which is defined as

$$\tilde{d} = d - f_d \max(0, d - C_{DES}\Delta) \quad (4)$$

with  $\Delta = \max(\Delta x, \Delta y, \Delta z)$  and  $f_d$  is the shielding function designed to be unity in the LES region and zero elsewhere.

The SA-neg model is the same as the “standard” version when the turbulence variable  $\tilde{\nu}$  is greater than or equal to zero. When the kinematic eddy viscosity would become negative, the Eq. 2 is modified, such that the turbulent eddy viscosity in the momentum and energy equations is set to zero [20].

### 3.2 Scale-adaptive approach

To only resolve turbulence where significant fluctuations exist, the work by Menter et al. [21] suggested a modified turbulence model which adds a source term  $Q_{SAS}$  based on the local von Karman length scale  $L_{vK}$  into the dissipation rate equation. This scale-resolving technique has been used in this study with the standard  $k-\omega$  SST model [22] as the base model in conjunction with the wall function technique. The governing equations of the SST-SAS model differ from the  $k-\omega$  SST model by the additional source

term  $Q_{SAS}$  in the transport equation for the turbulence eddy frequency  $\omega$  which is defined as shown in Eq. 5

$$Q_{SAS} = \max \left[ \rho \zeta_2 S^2 \left( \frac{L}{L_{vK}} \right)^2 - F_{SAS} \frac{2\rho k}{\sigma_\phi} \max \left( \frac{1}{k^2} \frac{\partial k}{\partial x_j} \frac{\partial k}{\partial x_j}, \frac{1}{\omega^2} \frac{\partial \omega}{\partial x_j} \frac{\partial \omega}{\partial x_j} \right), 0 \right] \quad (5)$$

with von Karman length scale  $L_{vK}$  given by

$$L_{vK} = \kappa \frac{U'}{U''}; \quad U'' = \sqrt{\frac{\partial^2 U_i}{\partial x_k^2} \frac{\partial^2 U_i}{\partial x_j^2}}; \quad U' = \sqrt{2 \cdot S_{ij} S_{ij}}$$

with  $k = 0.41$ ,  $\zeta_2 = 1.755$ ,  $\sigma_\phi = 2/3$ , and  $F_{SAS} = 1.25$ .

The SAS model can be considered as a scale-resolving URANS model, which can show LES-like behaviour. Unlike LES, it also remains well defined if the mesh cells get coarser and do not allow resolving scales well within the inertial range. This makes it attractive in the present application, where the aero-acoustic effects are mostly affected by larger turbulent scales which, in turn, need to be predicted accurately.

### 3.3 Wall functions approach

There are two classical wall boundary conditions, namely low-Re and high-Re type boundary conditions. The low-Re boundary condition imposes no-slip at the wall and requires a finer mesh. The aim of grid-independent wall functions is to provide a boundary condition at solid walls that enable flow solutions independent of the location of the first grid node above the wall. In this study, wall functions based on the universal law of the wall are employed for the DES-WF and SAS-WF simulations, whereas the low-Re boundary condition is used for the SAS simulation. The RANS equations are solved only down to the first grid node above the wall and are matched with an adaptive wall function solution at the first grid node above the wall. The matching condition (Eq. 6) makes sure that the wall-parallel components of the RANS solution and the wall function are equal at wall distance  $y_\delta$ , which is then solved for the friction velocity  $u_\tau$  using Newton's method. The shear stress  $\tau_\omega$  is then prescribed at the wall node

$$u_{RANS}(y_\delta) = u_{WF}(y_\delta). \quad (6)$$

In all the simulations, a second-order central scheme and backward Euler scheme have been used to discretize spatial flux and temporal terms, respectively. The time step size has been chosen, such that the convective Courant–Friedrichs–Lewy number (CFL) is well below 1.0.

## 4 Results and discussion

In this section, the experimental data will be first analysed and the effect of FFT window length will be determined to support the validation of the numerical simulations. Moreover, this section presents the physics of cavity flows including the validation of DES-WF, SAS, and SAS-WF simulations. The commonalities and differences between the used simulation methodologies will be highlighted and appropriate findings will be outlined.

### 4.1 Acoustic spectral analysis

In this subsection, first, the Rossiter modes are estimated using the semi-empirical model, which is then will be followed by the flow statistics with respect to prediction of the resonant modes by different simulation methodologies and RMS pressure.

#### 4.1.1 Theoretical estimation of Rossiter modes

The pressure signal that varies over a time series has been extracted along the cavity ceiling and transformed into frequency space to investigate the modes existing in the signal. Analytically, the frequencies at which the Rossiter modes occur can be computed through the Heller's modified Rossiter oscillation model (Eq. 7) [3]

$$f = \frac{U_\infty}{L} \frac{m - \alpha}{\text{Ma} / \left( \sqrt{1 + (\gamma - 1)\text{Ma}^2/2} \right) + 1/\kappa}. \quad (7)$$

#### 4.1.2 Effect of signal length on the RMS and FFT values

A total of 20.0s of pressure measurement data have been made available for the validation of simulation results. Prior to deciding on the length of the time series to be simulated, awareness of the effect of signal length on the FFT and RMS statistics is sought. To estimate this effect, some fundamental analysis of the raw data has been performed. The 20.0s of measurement data has been split into two groups of data: one group containing 160 samples of each 0.125s and the other group containing 40 samples of each 0.5s. Figure 3a shows the RMS pressure for both the sample groups. In the 0.125s case, the deviation in the RMS values is around 350 Pa near the front edge of the cavity between  $x/L = 0$  and  $x/L = 0.2$  and its value increases along the cavity length reaching around 500 Pa near  $x/L = 0.9$ . In the 0.5s case, the deviation in the RMS values is around 100 Pa near  $x/L = 0.2$  and increases to 350 Pa towards  $x/L = 0.9$ . Figure 3b shows the FFT

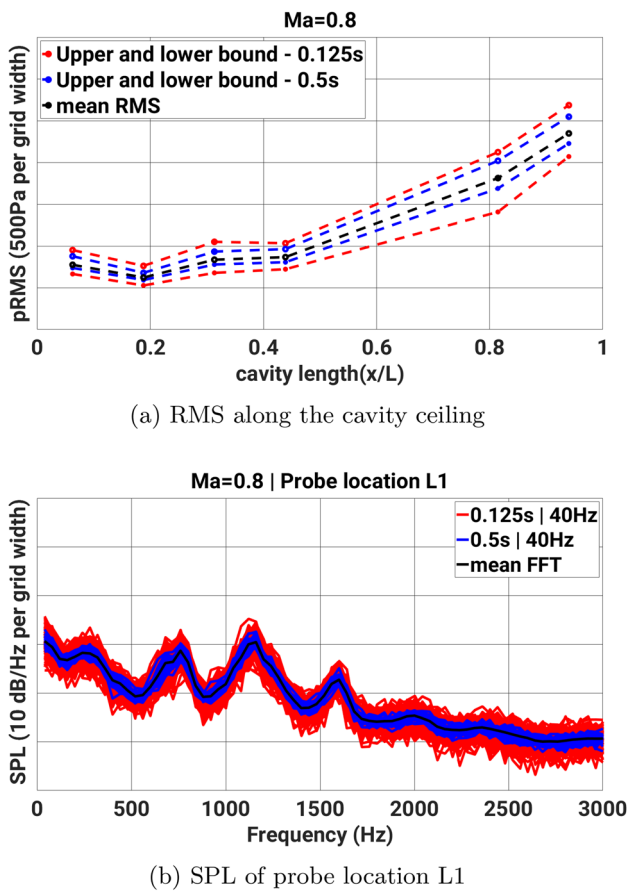
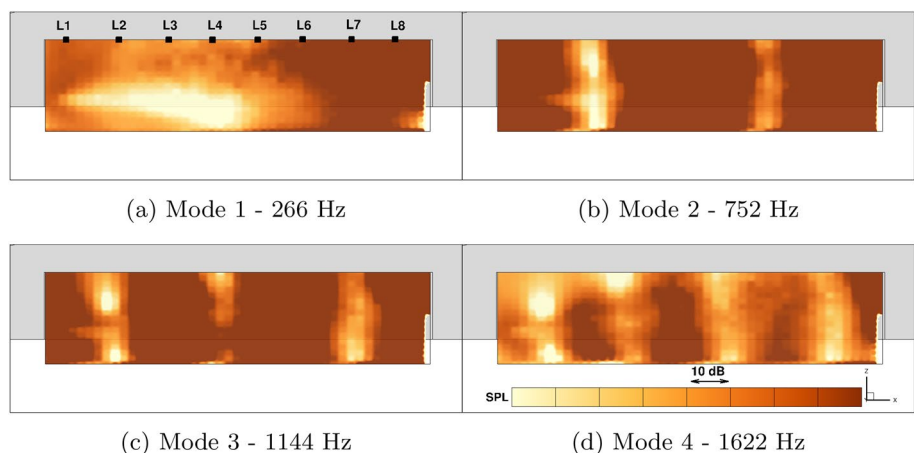


Fig. 3 Experimental data—effect of signal length on the RMS and FFT values

results of the two sample groups and displays that there is a variation of around 8–9 dB/Hz in the amplitude levels for 0.125s case, whereas the variation is around 4–5 dB/Hz for 0.5s case. This underlines the importance of selecting an appropriate signal length for the validation of the simulation data.

Fig. 4 SPL of the Rossiter modes predicted by DES-WF



### 4.1.3 Performance in terms of acoustic prediction

A fast Fourier transform (FFT) has been performed based on Welch’s method to decompose the pressure fluctuations into its frequency components. The input for the FFT has been the pressure data, which have been collected for over a 1000 locations on the mid-plane of the cavity. From all these locations, the amplitude of the first four resonance modes were identified and interpolated on the mid-plane to visualise the shape of the modes inside the cavity. The results can be seen in Fig. 4 showing the SPL distribution of the Rossiter modes 1,2,3 and 4 on the plane  $y = 0$ . Rossiter mode 1 has a node in the center of the cavity, anti-nodes on both ends and the front part is significantly overlaid by the shear layer, which suppresses the mode with its own frequency. The higher order Rossiter modes 2,3 and 4 correspond to the standing waves resulting from the organised vortical structures between the front and rear wall of the cavity. It is also observed that the lip of the cavity in all the modes is overlaid by the shear layer.

Figure 5 shows the FFT plots of experimental data, DES-WF, SAS, and SAS-WF simulations for the probe locations L1 and L8. From the experimental data in the FFT, the band with the group with samples of each 0.5 s is shown. Due to the expensive nature of the DES-WF simulation, the length of the series simulated in the DES-WF is 0.15s, whereas the length of series simulated in both the SAS and SAS-WF simulations is 0.25s. The time series of the simulations have been processed for the FFT analysis using the Hamming window function with the maximum offset length of FFT windows equivalent to the integral time scale computed through the autocorrelation function. The lowest frequency that the simulated data can resolve is kept around 40 Hz for all the simulations.

From the experimental data, the dominant modes of the probe locations L1 are 1, 2, and 3, whereas the dominant modes of L8 are 2 and 3. At the probe location L1, the mode 1 is predicted well by the DES-WF and SAS simulations.

Mode 2 is slightly over-predicted by the SAS simulation, whereas mode 3 is slightly underpredicted by the DES-WF simulation. The SAS-WF simulation tends to over-predict the modes, but shows the tendency to capture the frequencies as good as the DES-WF and SAS simulations.

As the pressure fluctuations are higher near the rear wall, it is worth to analyse the performance of the simulations with the FFT of the probe location L8. It is clearly seen that the SPL levels in general are higher in the probe location L8 as compared to the probe location L1. At the probe location L8, the mode 1 is captured quite well by the SAS simulation as compared to the DES-WF and SAS-WF simulations. The modes 2, 3, and 4 are captured adequately well by the DES-WF and SAS simulations. Although the DES-WF results slightly lie outside the experimental range formed by 0.5s samples, they show reasonable agreement in capturing the modes considering the length of the series simulated is 0.15s.

Table 1 shows the frequencies of the modes computed from modified Rossiter model and measured data together with the SAS simulation results. In the SAS simulations, the predicted modes fit extremely well with the frequencies of the experimental data and also with the theoretical modes, as shown in Table 1. In the probe location L1, the magnitude of the dominant mode is predicted well with a slight over-prediction of the modes 2. In the probe location L8, all the modes are predicted exceptionally well in terms of relative magnitudes, absolute magnitude, and the frequencies. Considering that severe pressure fluctuations exist towards the rear wall, the prediction of modes at the probe location L8 is extremely sensitive with higher SPL levels and the fact that the SAS simulation has captured the features of this location shows the reliability of the SAS simulation results.

In the SAS-WF simulation, the prediction of Rossiter frequencies still is quite good. It is observed that there is an offset by 3–4 dB/Hz when compared with SAS simulation results. Considering that the SAS-WF are 50% computationally cheaper than SAS simulations, the results seem quite promising.

To summarise the results, it is observed that the overall behaviour of all simulations is extremely good in terms of frequency prediction. However, the magnitude levels

between simulations show a noticeable difference. In particular, the SAS simulations fit the magnitude levels as good as the DES-WF simulations. The SAS-WF simulations show some good trends in predicting the modal frequencies and shapes with scope for improvement in its prediction capability.

#### 4.1.4 Performance in terms of RMS level prediction

Figure 6 shows the plot of root mean square (RMS) of pressure along the centerline of the cavity ceiling compared with the measured data. In DES-WF simulation, the predicted RMS of pressure fits the experimental data extremely well. In the SAS simulation, the predicted values fit the experimental data within the first 30% of the cavity length, over-predicted in the middle region, and captured reasonably well towards the rear portion. The reason for the over-prediction is related to the delayed prediction of the resolved structures in the shear layer (see Fig. 7). The activation of the  $Q_{SAS}$  term has been delayed and thereby the shear layer breakdown prediction shows a different behaviour than the DES-WF simulation. This delayed prediction of the shear layer has a consequent effect of higher fluctuations over the mid-section of the cavity. In the SAS-WF simulation, the RMS profile follows the trend of DES-WF simulation quite well but over-predicts the values significantly towards the regions of higher pressure RMS. The over-predicting behaviour of SAS-WF is also relatable to the distribution of the resolved turbulent kinetic energy, as shown in Fig. 7. The shear layer breakup has been considerably delayed compared to both the DES-WF and SAS simulations, and clearly, this has increased the scale of the fluctuations by a significant margin in the second half of the cavity.

## 4.2 Flow field visualisation

In this section, some of the flow features of the cavity, such as the resolution of the turbulent structures, boundary layer profile, and turbulent kinetic energy profile, are investigated and the performance of the simulations in terms of acoustic levels is discussed.

### 4.2.1 Visualisation of flow structures

To visualise the structures in the cavity configuration, the Q-criterion has been computed and it is shown in Fig. 8a. Attached boundary layer upstream of the cavity separates from the front edge and starts to shed vortices of varying scales. The vortical structures during their life time combine with other structures as they are convected downstream. After impinging on the rear wall of the cavity, some of the flow structures travel downstream after being ejected out and some travel upstream. Figure 8b shows the highly turbulent

**Table 1** Rossiter frequencies computed from theory, experiments, and the SAS simulation

Mode	Ma = 0.8		
	Theory (Hz)	Exp. (Hz)	CFD (Hz)
1	263	272	266
2	670	755	752
3	1076	1160	1144
4	1484	1600	1622

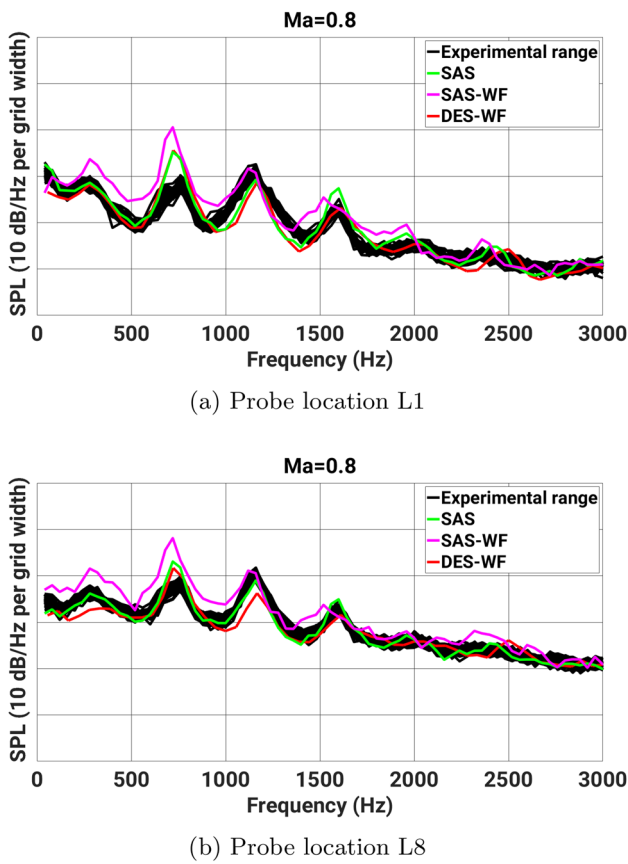


Fig. 5 FFT of experiment, DES-WF, SAS, and SAS-WF

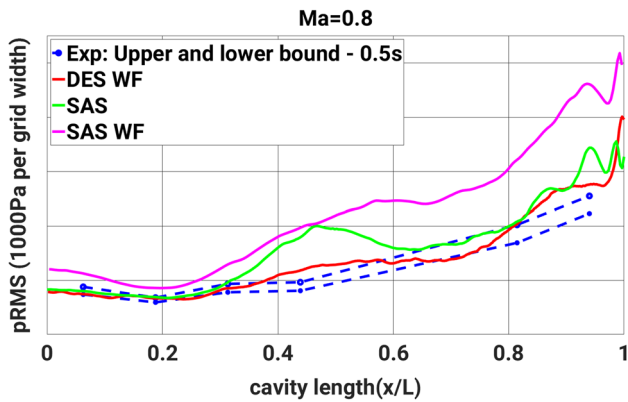


Fig. 6 RMS pressure of experiment, DES-WF, SAS, and SAS-WF

behaviour on the downstream corner of the cavity showing the flow redirecting from the rear wall and interacting with the oncoming shear flow components. Figure 8b shows a characteristic feature of an open-cavity configuration that the shear layer starts developing from the front edge as a

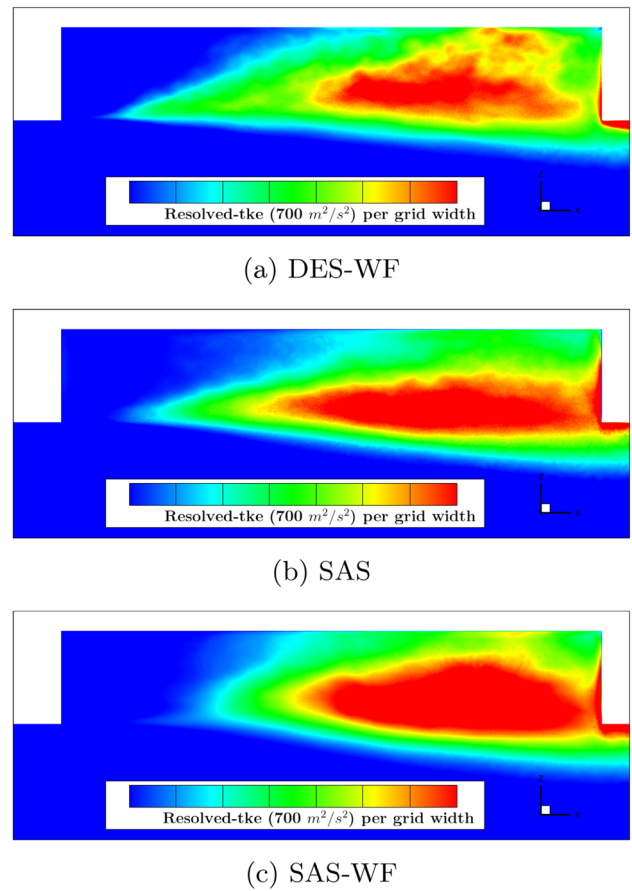


Fig. 7 Distribution of resolved turbulent kinetic energy at plane  $y = 0$

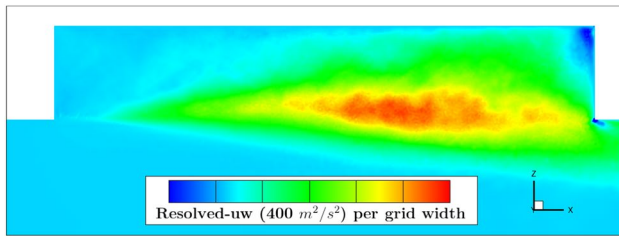
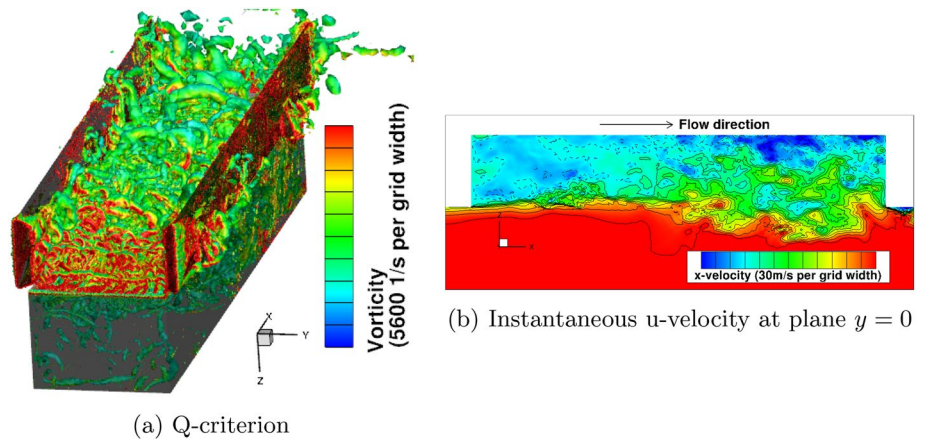
narrow region in the transverse direction and grows in the streamwise direction reaching its maximum width near the center of the cavity and reducing in width as the shear layer approaches the rear edge of the cavity. The prediction of shear layer width by the simulations is more clearly visible with the distribution of the resolved turbulent fluctuations in the streamwise and crosswise directions  $\overline{u'w'}$ , which is shown in Fig. 9. Furthermore, the distribution is such that the streamwise and crosswise velocity fluctuations are intense towards the aft wall in the case of SAS-WF simulation compared to the SAS simulation, while having maximum fluctuations inside the core of the shear layer.

#### 4.2.2 Turbulent flow field

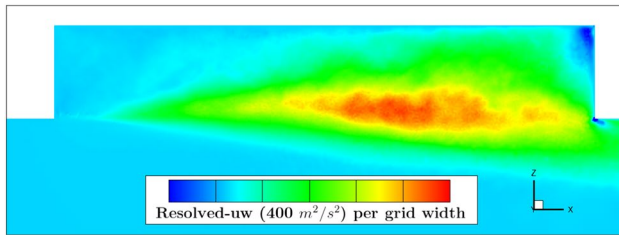
Figure 10 presents the flow field resolving capability of the DES-WF, SAS, and SAS-WF simulations inside the cavity by showing the vorticity magnitude in the plane  $y = 0$ . One can expect the flow field resolution from the DES-WF simulation to be high and this is indeed true as seen in Fig. 10a, which is used as a reference to investigate the resolving capability of the other turbulence models. Figure 10b shows



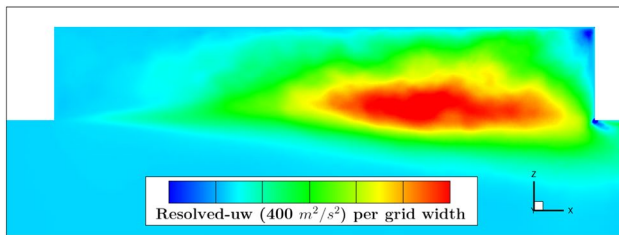
**Fig. 8** Visualisation of flow field inside the cavity using DES-WF simulation



(a) DES-WF



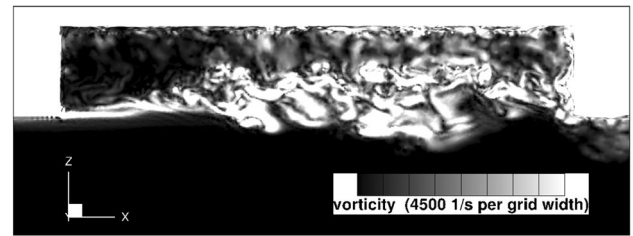
(b) SAS



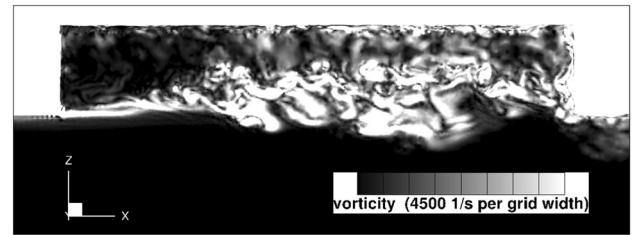
(c) SAS-WF

**Fig. 9** Distribution of Reynolds stress  $\overline{u'w'}$  at plane  $y = 0$

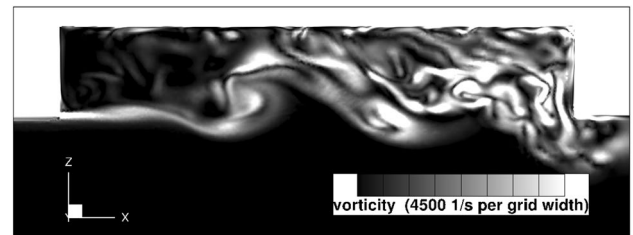
clearly not all the resolved scales as seen in the DES-WF simulation since the scale-resolving ability of the SAS model activates when there are enough unsteady fluctuations. Therefore, the structures are resolved in the shear layer and near the rear wall where the shear layer impinges



(a) DES-WF



(b) SAS



(c) SAS-WF

**Fig. 10** Instantaneous vorticity magnitude at plane  $y = 0$

and flows upstream. Figure 10c shows the flowfield snapshot from SAS-WF. The fine scale structures are clearly less pronounced than in the SAS simulation. The wall functions upstream of the wall did not produce resolved structures and this has led to the difference in the resolving capability of this variant.

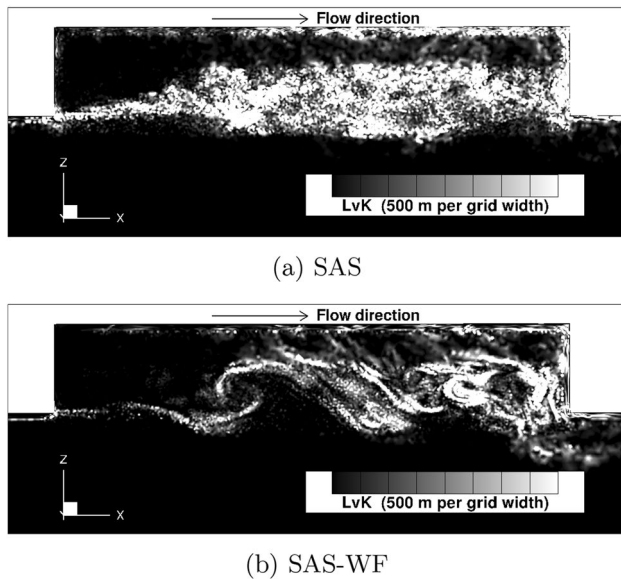


Fig. 11 von Karman Length scale,  $L_{vK}$  at plane  $y = 0$

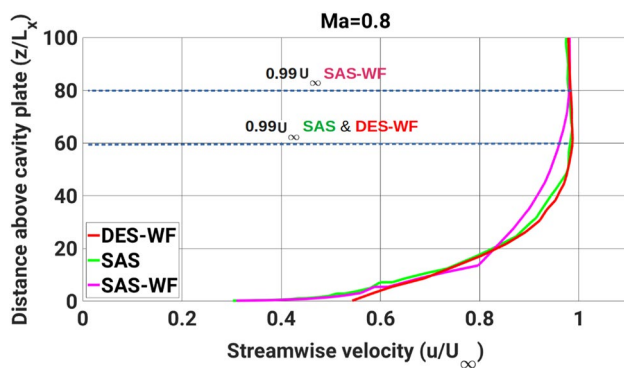


Fig. 12 Asymptotic near-wall profile ( $99\% U_\infty$ ) at a distance  $0.1L$  upstream of the cavity at plane  $y = 0$

#### 4.2.3 $L_{vK}$ prediction between SAS and SAS-WF

To further investigate the difference in the turbulent field resolution between SAS and SAS-WF simulations, the distribution of von Karman length scale has been investigated. The only difference between the SAS and SAS-WF meshes is the number of prism layers close to the wall. The SAS mesh has 35 prism layers with a  $y^+$  value less than 1.0, whereas the SAS-WF mesh has 10 prism layers with  $y^+$  value greater than 100. Therefore, it is noteworthy to investigate the von Karman length scale,  $L_{vK}$  predicted by SAS and SAS-WF simulations, as shown in Fig. 11, especially close to the walls. The von Karman length-scale represents a key element in triggering the model to allow the generation of resolved turbulence in Scale-Adaptive Simulations. As seen in Fig. 11, the  $L_{vK}$  is predicted strongly over a larger region

in the SAS simulation, whereas, in SAS-WF simulation, the region of  $L_{vK}$  presence is more limited. One can evidently observe that there is a difference near the upstream wall of the cavity between the two simulations. The authors believe that the usage of wall functions has rendered the SAS model to operate in pure RANS mode near the upstream wall of the cavity, which has led to the difference in the resolving capability of the model inside the cavity between SAS and SAS-WF simulations. If the model had operated in the resolving mode close to the front edge of the cavity, the SAS-WF could have better predicted the shear layer growth and its breakdown as observed in SAS and DES-WF simulations.

In Fig. 12, the asymptotic near-wall flow profile at  $0.1L$  distance upstream of the cavity has been shown. It is noticed that as a result of RANS behaviour close to the wall without resolved structures, the thickness of the boundary layer based on the  $99\% U_\infty$  measure in SAS-WF simulation is larger than the thickness predicted by the DES-WF and SAS simulations. The boundary layer developed upstream of the cavity has an important effect on the growth of the shear layer. Most, if not all of eddy viscosity contained in the boundary layer is transferred to the shear layer making it more stable than in the DES-WF and SAS simulations. This thicker shear layer with higher turbulent energy content cannot breakdown sooner as seen in the SAS simulation and the process of shear layer breakdown is thereby delayed, as the shear layer contains most of the energy-carrying eddies and they do not dissipate enough energy. This leads to over-prediction of energy levels inside the cavity as seen in Figs. 5 and 6. Moreover, the predicted shape factor (i.e., the ratio of displacement to momentum thickness) has been determined as 1.24 in the case of DES-WF simulation at a distance  $0.1L$  upstream of the cavity, having the local  $Re_x = 2.8 \times 10^6$ . Further, it is observed that with respect to the DES-WF case, there is a nominal over-prediction of 5–10% in the displacement and momentum thicknesses in the SAS simulation, whereas around 20% over-prediction is found in the case of the SAS-WF simulation, both showing deviations of the shape factor as low as 3% from the DES-WF case. Finally, the  $99\%$  thickness for the DES-WF reference case has been found to be  $60L_x$  which coincides with the SAS prediction.

Figure 13 further confirms presence of more energy inside the cavity by showing the mean turbulent kinetic energy profile for four slices at  $x/L = 0.19, 0.37, 0.56$  and  $0.94$ . It is evident that the turbulent kinetic energy produced by SAS-WF simulation is higher than in the SAS simulation. The thicker boundary layer profile in SAS-WF has transferred most of its energy to the shear layer, and therefore, turbulent kinetic energy is maximal at the cavity lip. Further downstream, at locations  $x/L = 0.56$  and  $x/L = 0.94$ , more energy is seen transferred inside the cavity in the SAS-WF simulation, which leads to higher pressure fluctuations in SAS-WF as seen in Fig. 6.

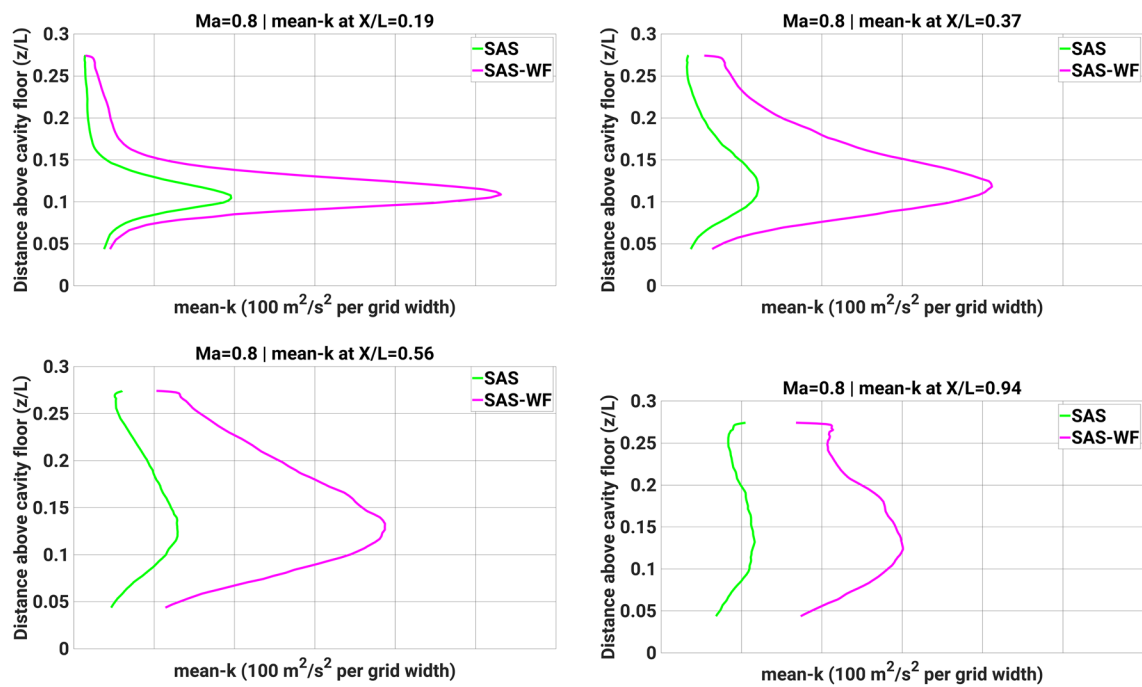


Fig. 13 Time-averaged modelled turbulent kinetic energy at plane  $y = 0$

## 5 Conclusion and outlook

In this study, a novel cavity configuration with sidewise doors has been studied numerically with three simulation methodologies such as DES with wall functions (DES-WF) and SAS with wall resolved and using wall functions (SAS and SAS-WF) under the transonic flow conditions of  $Ma$  0.8 and  $Re$   $12 \times 10^6$ . The correlation of the Rossiter modes with the flow processes has been identified in detail through FFT of DES-WF simulation results. It has been proven that all three simulation methodologies can capture the Rossiter frequencies well with a marginal over-prediction of spectral magnitudes by the SAS-WF simulation. The reason for the over-prediction behaviour in the SAS-WF simulation has been investigated with the boundary layer profile and the resolved fluctuations inside the cavity. The commonalities and differences between SAS and SAS-WF simulations were investigated and outlined using the von Karman length scale and vorticity fields. On the requirements of computational cost, the DES-WF simulation is estimated to be around 50% computationally cheaper than the wall-integrated DES simulation, whereas the SAS simulation is estimated to be 90% faster than DES simulations and the SAS-WF simulation is twice as fast as the SAS simulation. As the cheapest of the three simulations that were carried out in this study, the SAS-WF shows good trends in predicting the modal frequencies and shapes. The reasons for a moderate over-prediction behaviour have been investigated and outlined in this study. To overcome these numerical issues

in SAS-WF simulations, future work will address the breakdown phenomena of shear layer in detail by incorporating a synthetic turbulence forcing term.

**Funding** Open Access funding enabled and organized by Projekt DEAL. This work has been carried out with the financial support from Airbus Defence and Space (ADS) under the project “Analysis of Unsteady Effects in Fighter Aircraft Aerodynamics”, which is greatly acknowledged. The authors would like to thank the German Aerospace Center (DLR) for providing the TAU code and Ennova Technologies, Inc. for the meshing software. The authors would also like to acknowledge the Gauss Centre for Supercomputing for making the required computing hours available to this study.

**Data availability** Datasets generated during the study can be made available by the corresponding author upon request.

**Declaration**

**Conflict of interest** The authors have no competing interests to declare that are relevant to the content of this article.

**Open Access** This article is licensed under a Creative Commons Attribution 4.0 International License, which permits use, sharing, adaptation, distribution and reproduction in any medium or format, as long as you give appropriate credit to the original author(s) and the source, provide a link to the Creative Commons licence, and indicate if changes were made. The images or other third party material in this article are included in the article's Creative Commons licence, unless indicated otherwise in a credit line to the material. If material is not included in the article's Creative Commons licence and your intended use is not permitted by statutory regulation or exceeds the permitted use, you will

need to obtain permission directly from the copyright holder. To view a copy of this licence, visit <http://creativecommons.org/licenses/by/4.0/>.

## References

1. Lawson, S.J., Barakos, G.N.: Review of numerical simulations for high-speed, turbulent cavity flows. *Prog. Aerosp. Sci.* **47**(3), 186–216 (2011). <https://doi.org/10.1016/j.paerosci.2010.11.002>
2. Rossiter, J.E.: Wind tunnel experiments on the flow over rectangular cavities at subsonic and transonic speeds. <http://repository.tudelft.nl/view/aereports/uuid:a38f3704-18d9-4ac8-a204-14ae03d84d8c/> (1964)
3. Heller, H.H., Holmes, D.G., Covert, E.E.: Flow-induced pressure oscillations in shallow cavities. *J. Sound Vib.* **18**, 545–553 (1971)
4. Handa, T., Miyachi, H., Kakuno, H., Ozaki, T., Maruyama, S.: Modeling of a feedback mechanism in supersonic deep-cavity flows. *AIAA J.* **53**(2), 420–425 (2015). <https://doi.org/10.2514/1.J053184>
5. Henschaw, M.J.d.C.: M219 Cavity Case in Verification and Validation Data for Computational Unsteady Aerodynamics, vol. 323 (2000)
6. Henderson, J., Badcock, K., Richards, B.E.: Subsonic and transonic transitional cavity flows. In: 6th Aeroacoustics Conference and Exhibit. <https://doi.org/10.2514/6.2000-1966> (2000)
7. Allen, R., Mendonca, F., Kirkham, D.: RANS and DES turbulence model predictions on the M219 cavity at  $M=0.85$ . In: RTO AVT Symposium, vol. 18 (2004)
8. Chang, K., Constantinescu, G., Park, S.O.: Assessment of predictive capabilities of detached eddy simulation to simulate flow and mass transport past open cavities. *J. Fluids Eng. Trans. ASME* **129**(11), 1372–1383 (2007). <https://doi.org/10.1115/1.2786529>
9. Woo, C., Kim, J., Lee, K.: Three-dimensional effects of supersonic cavity flow due to the variation of cavity aspect and width ratios. *J. Mech. Sci. Technol.* **22**(3), 590–598 (2008). <https://doi.org/10.1007/s12206-007-1103-9>
10. Larchevêque, L., Sagaut, P., Labbé, O.: Large-eddy simulation of a subsonic cavity flow including asymmetric three-dimensional effects. *J. Fluid Mech.* **577**(July 2019), 105–126. <https://doi.org/10.1017/S0022112006004502> (2007)
11. Menter, F.R., Egorov, Y.: The scale-adaptive simulation method for unsteady turbulent flow predictions. Part 1: theory and model description. *Flow Turbulence Combust.* **85**(1), 113–138 (2010). <https://doi.org/10.1007/s10494-010-9264-5>
12. Girimaji, S., Werner, H., Peng, S., Schwaborn, D.: Progress in Hybrid RANS-LES Modelling. *Methods* **130**, 19–21 (2015)
13. Mayer, F., Mancini, S., Kolb, A.: Experimental Investigation of Installation Effects on the Aeroacoustic Behaviour of Rectangular Cavities at High Subsonic and Supersonic Speed. Deutscher Luft- und Raumfahrtkongress (2020)
14. Langer, S., Schwöppe, A., Kroll, N.: The DLR flow solver TAU—status and recent algorithmic developments. In: 52nd Aerospace Sciences Meeting. <https://doi.org/10.2514/6.2014-0080> (2014)
15. Chaouat, B.: The State of the Art of Hybrid RANS/LES modeling for the simulation of turbulent flows. *Flow Turbul. Combust.* **99**(2), 279–327 (2017). <https://doi.org/10.1007/s10494-017-9828-8>
16. Rajkumar, K., Tangermann, E., Klein, M., Ketterl, S., Winkler, A.: DES of weapon bay in fighter aircraft under high-subsonic and supersonic conditions. *Notes Numer. Fluid Mech. Multidiscip. Des.* **151**, 656–665 (2021). [https://doi.org/10.1007/978-3-030-79561-0\\_62](https://doi.org/10.1007/978-3-030-79561-0_62)
17. Spalart, P.R., Jou, W.H., Strelets, M., Allmaras, S.R.: Comments on the feasibility of LES for wings and on a hybrid RANS/LES approach. *Adv. DNS/LES* **1**(January), 4–8 (1997)
18. Spalart, P.R., Allmaras, S.R.: A one-equation turbulence model for aerodynamic flows. *La Recherche aérospatiale* **1**, 5–21 (1994). <https://doi.org/10.2514/6.1992-439>
19. Shur, M.L., Spalart, P.R., Strelets, M., Travin, A.K.: A hybrid RANS-LES approach with delayed-DES and wall-modelled LES capabilities. *Int. J. Heat Fluid Flow* **29**(6), 1638–1649 (2008). <https://doi.org/10.1016/j.ijheatfluidflow.2008.07.001>
20. Rumsey, C.L.: The Spalart-Allmaras Turbulence Model, Turbulence Modeling Resource. NASA Langley Research Center (2021)
21. Menter, F.R., Garbaruk, A., Smirnov, P., Cokljat, D., Mathey, F.: Scale-adaptive simulation with artificial forcing. *Notes Numer. Fluid Mech. Multidiscip. Des.* **111**(January), 235–246 (2010). [https://doi.org/10.1007/978-3-642-14168-3\\_20](https://doi.org/10.1007/978-3-642-14168-3_20)
22. Menter, F.R.: Two-equation eddy-viscosity turbulence models for engineering applications. *AIAA J.* **32**(8), 1598–1605 (1994). <https://doi.org/10.2514/3.12149>